Analysis and Real-Time Calculation of Postfault Current of Standard Surface-Mounted PMSM Drives With Dysfunctional Power Switches

Zeliang Zhang, *Student Member, IEEE*, Yihua Hu, *Senior Member, IEEE*, Guangzhao Luo, *Senior Member, IEEE*, Hui Xu, and Chao Gong, *Member, IEEE*

***Abstract*—Fault diagnosis and fault-tolerant control significantly rely on the knowledge of fault mechanisms and postfault states. Regarding open circuits in permanent magnet synchronous motor drives, the postfault states, especially phase voltages, depend on whether the faulty phase is conducting. Under the open-switch fault featuring dysfunctional power switches, the faulty phase is possible to conduct through the still functional diodes. In contrast, the open-phase fault completely blocks the faulty phase. However, the mechanism and effects of the open-switch conduction have not been thoroughly studied, which obscures the boundary between the open-switch fault and the open-phase fault, and fails to realize effective diagnosis and optimal fault-tolerant control. This article not only reveals the mechanism of the open-switch conduction, but also proposes a model that can calculate the postfault conducting current in real time. The proposed model provides an estimation value of the postfault current for further utilization and validates the correctness of the analysis. First, equivalent circuits are analyzed to explain the conduction condition. Subsequently, switching states fulfilling the conditions are studied, and finally, the mathematical model of the postfault current is built. The analysis and model are experimentally validated.**

***Index Terms*—Open circuits, permanent magnet synchronous motor (PMSM), power switches.**

I. Introduction

IN THE development of the permanent magnet synchronous motor (PMSM) and its drive, high reliability has always been one of the major concerns. Among the components in a PMSM drive, the power inverter is susceptible to interferences and is considered the most fragile component by 31% of the responders in an industry-based survey [1]. From the phenomenon viewpoint, inverter faults can be categorized into two phenomena: open circuit and short circuit, and the open circuit occurs more often [2] and has been attracting more attention [3], [4].

The open-circuit phenomenon can be incurred by different types of faults, the most typical of which are the open-switch fault and open-phase fault. The open-switch fault is attributed to failures on the inverter side, including damaged power switches, missing driving signals incurred by the bonding wire, and driver failures. In addition, the open-switch fault can also be a result of the short-circuit protections. Attributing to the sophisticated protection design [5], short circuits [6] can be assuredly converted to open circuits. In most designs, the short-circuit protection is secured by comparator-based circuits integrated into driving chips and the protection algorithm integrated into the software. Meanwhile, the open-phase fault is on the motor side and results from the damaged motor winding and connection failure of power cables or connectors. In addition, the postfault current of the open-switch fault is nonzero due to the antiparallel diodes, while the open-phase fault completely blocks the current path.

In terms of diagnosis, the model-based method compares feedback values and estimated values acquired from explicit physical models [7], [8]. Comparatively, the data-driven method emphasizes statistical significance and is suitable for uncertain or complex targets [9], [10]. Additionally, fault-tolerant control relies on the system model to reconfigure redundant systems [11], [12] or reconstruct the control of nonredundant systems [3], [13]. The open-switch fault in this article is incurred by missing driving signals due to power device failures or driver failures [4] and should be distinguished from open-phase faults [14], [15], where the postfault current is zero.

Distinguishing the open-switch fault and open-phase fault is necessary for the fault-tolerant control and maintenance of the PMSM drive:

a) To realize effective fault-tolerant control, the postfault model must be determined. The fault-tolerant control reconfigures the implementation of voltage vectors based on prefault and postfault phase voltages [13], [16]. However, the open-switch and open-phase faults have different postfault phase voltages. The phase voltages are fixed under the open-switch fault where the diodes of the faulty phase

Manuscript received 4 November 2022; revised 13 March 2023; accepted 16 May 2023. Date of publication 19 May 2023; date of current version 21 June 2023. This work was supported in part by the EPSRC under Grant EP/W006308/1 and in part by China Scholarship Council. Recommended for publication by Associate Editor F. Khan.*(Corresponding author: Yihua Hu.)*

Zeliang Zhang is with the Department of Electronic Engineering, University of York, YO10 5DD York, U.K. (e-mail: 18829237032@163.com).

Yihua Hu is with the Department of Engineering, King's College London, WC2R 2LS London, U.K. (e-mail: yihua.hu@york.ac.uk).

Guangzhao Luo is with the School of Automation, Northwestern Polytechnical University, Xi'an 710072, China (e-mail: guangzhao.luo@nwpu.edu.cn).

Hui Xu is with the Leeds Beckett University, LS1 3HE Leeds, U.K. (e-mail: hui.xu@york.ac.uk).

Chao Gong is with the Department of Electrical and Computer Engineering, University of Alberta, Edmonton, AB T6G 2R3, Canada (e-mail: 1452101806@qq.com).

Color versions of one or more figures in this article are available at https://doi.org/10.1109/TPEL.2023.3277913.

Digital Object Identifier 10.1109/TPEL.2023.3277913

are conducting; otherwise, the phase voltages float when the diodes are blocked or under the open-phase fault. Different phase voltages result in different strategies of the postfault modulation method. Hence, distinguishing the open-switch and open-phase faults is critical for fault-tolerant control.

b) Distinguishing the two faults facilitates the maintenance of the motor drive and brings the fault diagnosis of open circuits to a more detailed level. The open-switch fault on the inverter side is incurred by the nonconduction of power switches, while the open-phase fault results from connection failures on connectors, terminals, or motor windings. Distinguishing an open-switch fault from an open-phase fault can narrow the scope of fault obviation and save time on maintenance.

To distinguish the open-switch fault and open-phase fault, the nonzero postfault current of the open-switch fault needs to be sampled and estimated for model-based methods. However, on the one hand, the open-switch fault model must be developed for estimating the postfault current in real time; on the other hand, the nonzero current conducts in specific switching states, and the normal current sampling cannot detect it intact.

The nonzero current of the open-switch fault in an induction motor drive was reported in [17] by experiments and cosimulation. The fault-tolerant control of the induction motor drive was improved in [18] by considering the effect of the nonzero current on phase voltages. In [16], the effect of the nonzero current on phase voltages was considered in the fault-tolerant control of a PM generator. A similar modeling method was expanded to multiple open-switch faults in a PMSM drive in [19]. Moreover, the nonzero postfault current was exploited to realize sensorless control under open-circuit faults [20] in which the rotor position was derived from the sampled nonzero postfault current. Since the nonzero current is activated in special switching states instead of all of them, the sampling points should be specifically arranged according to the mechanism of the nonzero current.

Although the effect of the postfault conduction on the phase voltages can be determined by comparing it with the prefault switching states, the faulty phase is not always being conducted by every switching state but only by specific switching states which have not been revealed. Furthermore, no model has been established to explain the mechanism of the postfault current and estimate its value for further utilization. The estimation of the open-switch postfault current can be employed not only in model-based diagnosis methods but also in correcting or deriving the rotor position since the postfault current is determined by the back-electromagnetic force. To estimate the postfault current, the switching states that activate the postfault current must be revealed. On the one hand, the acting time of the specific switching states is the conduction time of the postfault current; on the other hand, the switching states determine the postfault equivalent circuits, which determine the voltage source of the postfault current. Therefore, the postfault conduction should be studied on the scale of the switching period.

Besides, it should be noted that the studied open-circuit current is different from the current generated when the motor works as a generator. The uncontrolled generation (UCG) current was thoroughly studied in [21] and has the following differences compared with the studied open-circuit current:

1) Unlike the UCG current, which flows back to the dc source with amplitudes ranging from tens to hundreds of amperes, the studied open-circuit current flows within the motor drive and is in the milliampere range. This is because the open-circuit current is not only related to the back-EMF, but also to the acting time of its activating switching states.
2) The UCG current is not related to the switching states of the inverter, while the open-circuit current can only be activated by its activating switching states.
3) Unlike the UCG current that feeds power to the power source, the open-circuit current does not feed power but can be employed for various purposes such as diagnosis, fault-tolerant control, and parameter estimation.

This article aims to reveal the mechanism of the postfault conduction on the scale of the switching period and precisely estimate the postfault nonzero current in real time by the following steps:

1) First, in Section II-A, the conduction conditions of the upper diode and lower diode are separately analyzed at different speed levels. The conduction condition is the most important factor that determines the sign of the postfault current and the required connecting states of the inverter.
2) Based on the conduction conditions and connecting states required to realize the conduction conditions, in Section II-B, the switching states qualifying to conduct the faulty phase are revealed, according to the polarity and amplitude of the back-electromagnetic force determined by the motor speed. Furthermore, the conduction time of the postfault current is summarized in Table I by considering the acting time of voltage vectors and the dead time of power switches.
3) After obtaining the conduction time, an estimation model of the postfault current is proposed based on the equivalent circuits that correspond to the connecting states of the switching states. The estimation model can accurately calculate the postfault current at different speed levels on the scale of hundreds of milliamperes.
4) Finally, in Section III, the analysis of the conduction conditions and conduction time, current and voltage dynamics, and estimation model are validated in experiments.

TABLE I
CONDUCTION TIME OF D_1 AND D_2

	$0<V_{bemfa}<\frac{V_{DC}}{3}$	$\frac{1}{3}V_{DC}<V_{bemfa}$			
Sector	V, VI, I, II	V	VI	I	II
Δt_{D1}	T_{u7}-T_d	T_{u7}-T_d+ T_{u1}+T_{u5}	T_{u7}-T_d +T_{u5}	T_{u7}-T_d +T_{u6}	T_{u7}-T_d + T_{u6}+T_{u2}
	$0>V_{bemfa}>\frac{-V_{DC}}{3}$	$-\frac{1}{3}V_{DC}>V_{bemfa}$			
Sector	II, III, IV, V	II	III	IV	V
Δt_{D2}	T_{u0}+T_d	T_{u0}+T_d+ T_{u2}+T_{u6}	T_{u0}+T_d +T_{u2}	T_{u0}+T_d +T_{u1}	T_{u0}+T_d+ T_{u1}+T_{u5}

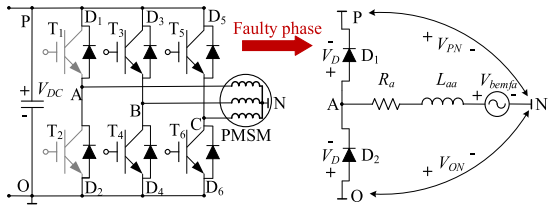

Fig. 1. Postfault schematic and phase-A equivalent circuit.

In the analysis and experiments of this case, to comprehensively study both polarities of the postfault current, two open-switch faults in the same inverter leg are analyzed and implemented.

II. Mechanism of Open-Circuit Current Conduction

A. Analysis of the Open-Circuit Conduction Conditions

When the motor drive is healthy, the rotor synchronous frame provides the convenience of transforming the symmetric three-phase states to the decoupled *dq* states. However, after the occurrence of the fault, the three-phase states are no longer symmetric and the transformed *dq* states are also coupled by the electric angle. To identify the open-circuit conduction conditions, the three-phase voltages need to be independently analyzed in combination with the three-phase switching state. Therefore, the three-phase independent analysis is more suitable for deducing the open-circuit postfault conduction.

When no fault occurs, the phase-A current is determined by both the power source and back-electromagnetic force and can be described by the voltage equilibrium equation:

$$\begin{aligned} u_{an} &= R_a i_a + d\Psi_a/dt \\ &= R_a i_a + L_{aa}\frac{di_a}{dt} + L_{ab}\frac{di_b}{dt} + L_{ac}\frac{di_c}{dt} - \Psi_f \omega_e \sin\theta_e \end{aligned} \tag{1}$$

where u_{an}, R_a, i_a, Ψ_a, and L_{aa} are the voltage, resistance, current, flux linkage, and self-inductance of phase A; i_b, i_c, L_{ab}, and L_{ac} are the currents of phases B and C and mutual inductances; Ψ_f, θ_e, and ω_e are the rotor flux linkage, electrical angle, and velocity, respectively. The last item of (1) is defined as the back-electromagnetic force V_{bemfa}, and its polarity is described in (2) when ω_e is positive.

$$V_{bemfa} = -\Psi_f \omega_e \sin\theta_e \begin{cases} > 0, \theta_e \in (\pi, 2\pi) \\ < 0, \theta_e \in (0, \pi) \end{cases}. \tag{2}$$

Assuming that the open-switch faults occur in phase A, the postfault schematic and equivalent circuit are shown in Fig. 1, where V_D is the forward on-voltage of the reverse diode. V_{bemfa} acts as the only potential source of the nonzero current because a) V_{dc} has been blocked by the antiparallel diodes and b) the postfault currents of phases B and C have reverse polarities but almost identical amplitudes; thus, the voltages induced by mutual inductances are mutually canceled. Moreover, the conduction of the faulty phase depends on the voltage differences between the neutral point of the stator winding N and power source rails, viz. V_{PN} and V_{ON}.

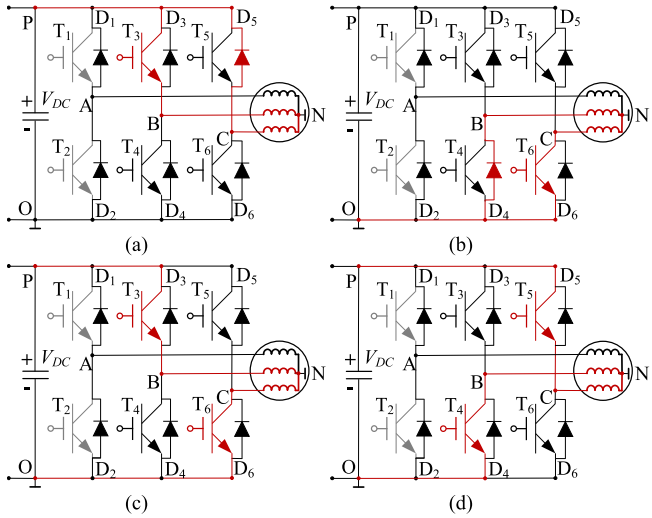

Fig. 2. Postfault conduction paths that connect phases B and C (a) to the positive rail, (b) to the negative rail, and (c) and (d) to the positive and negative rails separately.

When $V_{bemfa} > 0$ V, D_1 can conduct, while D_2 is intrinsically reverse-biased by the negative rail and V_{bemfa} positive polarity. According to Fig. 1, D_1 can be conducted if the voltage difference V_{AP} can cover V_D. Before the conduction of D_1, V_{bemfa} is the only voltage source of phase A since its current is still 0 before its conduction. Hence, the conduction condition of D_1 can be described as follows:

$$V_{AP} = V_{AN} - V_{PN} = V_{bemfa} - V_{PN} > V_D. \tag{3}$$

V_D can be neglected compared with V_{bemfa} and V_{PN}. For example, in terms of the experimental setup of this case, V_D is 1.5 V and can be easily covered by V_{bemfa} if the motor speed is higher than 25 rpm, which is far less than its nominal speed.

B. Inverter Connections of the Postfault Current Conduction

In (3), V_{PN} determines the conduction of D_1 and it is necessary to study the state of V_{PN} before the conduction of D_1. Since the driving signals of the faulty phase are invalid under the open-switch fault, possible connecting states before the D_1 conduction are shown in Fig. 2.

The state of V_{PN} and its relationship with V_{bemfa} will be separately discussed according to the above states. In the four states of Fig. 2, because D_1 has not been conducted, the following equations of phase currents hold true: $i_a = 0$ and $i_b = -i_c$, and the relationship of the phase voltages: $V_{AN} + V_{BN} + V_{CN} = 0$. In Fig. 2(a) and (b), because both phases B and C are connected to the dc rails, the line-to-line voltage is $V_{BC} = 0 = V_{BN} - V_{CN}$. Applying it to $V_{AN} + V_{BN} + V_{CN} = 0$, their phase voltages can be expressed as follows:

$$V_{BN} = V_{CN} = \frac{-V_{AN}}{2} = \frac{-V_{bemfa}}{2}. \tag{4}$$

In Fig. 2(a), $V_{PN} = V_{BN} = V_{CN} = -V_{bemfa}/2$, and the condition in (3) is transferred to

$$V_{AP} = V_{AN} - V_{PN} = V_{AN} - \left(-\frac{V_{bemfa}}{2}\right) = \frac{3V_{bemfa}}{2} > 0. \tag{5}$$

The condition in (5) can be achieved by V_{bemfa} at all speed levels. Hence, D_1 can be conducted by connecting phases B and C to the positive rail.

Comparatively, in Fig. 2(b), $V_{ON} = V_{BN} = V_{CN} = -V_{bemfa}/2$, and V_{PN} can be obtained from

$$V_{PN} = V_{PO} + V_{ON} = V_{dc} - \frac{V_{bemfa}}{2}. \tag{6}$$

The condition in (3) can be transferred to

$$V_{AP} = V_{AN} - V_{PN} = \frac{3V_{bemfa} - 2V_{dc}}{2} > 0 \tag{7}$$

$V_{bemfa} > (2V_{dc}/3)$ is required to satisfy (7). However, $V_{bemfa} > (2V_{dc}/3)$ cannot be achieved in a standard PMSM drive. $(2V_{dc}/3)$ is the maximum instant value that the phase voltage can reach in a three-phase two-level inverter. For example, $V_{AN} = (2V_{dc}/3)$ when $\overrightarrow{u_4}(100)$ is being applied. According to the pulsewidth modulation (PWM) method, the phase voltage is the synthesized voltage-second value of the instant phase voltage V_{AN} and its acting time. Considering the principle of space vector PWM (SVPWM) and the effect of the dead time, the acting time of the instant value $(2V_{dc}/3)$ does not account for the entire switching cycle. Therefore, the phase voltage cannot reach $(2V_{dc}/3)$. Furthermore, according to the phase voltage equilibrium, the phase voltage is equal to the summary of V_{bemfa} and voltage drops on the resistance and inductance. Hence, V_{bemfa} cannot reach $(2V_{dc}/3)$, and connecting phases B and C to the negative rail cannot conduct D_1.

In Fig. 2(c) and (d), by introducing $V_{BC} = V_{dc} = V_{BN} - V_{CN}$ and $V_{BC} = -V_{dc} = V_{BN} - V_{CN}$ to $V_{AN} + V_{BN} + V_{CN} = 0$, we obtain

$$V_{BN} = \frac{V_{dc} - V_{bemfa}}{2} = V_{PN};$$
$$V_{CN} = \frac{-V_{dc} - V_{bemfa}}{2} = V_{ON}, \text{Fig.2}(c) \tag{8}$$
$$V_{BN} = \frac{-V_{dc} - V_{bemfa}}{2} = V_{ON};$$
$$V_{CN} = \frac{V_{dc} - V_{bemfa}}{2} = V_{PN}, \text{Fig.2}(d). \tag{9}$$

The condition in (3) can be transferred as follows:

$$V_{AP} = V_{AN} - V_{PN} = \frac{3V_{bemfa} - V_{dc}}{2} > 0. \tag{10}$$

Equation (10) shows that D_1 can be conducted by separately connecting phases B and C to the positive and negative rails at high speed levels if the following condition is satisfied

$$V_{bemfa} > \frac{V_{dc}}{3}. \tag{11}$$

When $V_{bemfa} < 0$, D_2 has the potential to conduct, but the condition in (3) has changed to

$$V_{OA} = V_{ON} - V_{AN} = V_{ON} - V_{bemfa} > 0. \tag{12}$$

By applying the same analysis, the conduction condition in (12) is discussed according to the four connecting states in Fig. 2 as follows:

a) In Fig. 2(a), $V_{ON} = V_{OP} + V_{PN} = -V_{dc} - V_{bemfa}/2$, and the condition in (12) is transferred to

$$V_{OA} = V_{ON} - V_{AN} = -\frac{(3V_{bemfa} + 2V_{dc})}{2} > 0. \tag{13}$$

Similar to the condition in (7), $V_{bemfa} < -(2/3)V_{dc}$ is required and cannot be achieved. Therefore, D_2 cannot be conducted by connecting phases B and C to the positive rail.

a) In Fig. 2(b), the condition in (12) is transferred to

$$V_{OA} = V_{ON} - V_{AN} = -\frac{3V_{bemfa}}{2} > 0. \tag{14}$$

The condition in (14) can be achieved at all speed levels. Therefore, D_2 can be conducted at all speed levels by connecting phases B and C to the negative rail.

a) In Fig. 2(c) and (d), the condition in (12) has been transferred to

$$V_{OA} = V_{ON} - V_{AN} = -\frac{(3V_{bemfa} + V_{dc})}{2} > 0. \tag{15}$$

At high speed levels where $V_{bemfa} < -(V_{dc}/3)$, D_2 can be conducted by separately connecting phases B and C to the positive rail and negative rail.

III. Activating Switching States and Estimation Model of the Open-Circuit Current

A. Identifying Activating Switching States and Conduction Time of the Open-Circuit Current

Because the conduction of the nonzero current is determined by the polarity of V_{bemfa} and connecting states in Fig. 2, the switching states that correspond to each polarity of V_{bemfa} and each condition in Fig. 2 will be discussed before analyzing the conduction time of the nonzero current. Conventional field-oriented control (FOC) performs the *dq*-coordinate transformation based on the rotor electrical angle θ_e and aligns the direction of flux control to the rotor flux. An alternative to the conventional FOC oriented to the rotor flux is the stator flux FOC, which aligns the rotating reference to the stator flux [22], [23]. Therefore, θ_e determines the polarity of V_{bemfa} and is orthogonal to the voltage vector synthesized by two adjacent vectors in each spatial sector. The voltage vectors and polarity of V_{bemfa} are depicted in Fig. 3, where "1" denotes the active power switch of the upper leg and inactive power switch of the lower leg, while "0" denotes the opposite.

As previously analyzed, if $V_{bemfa} > 0$, D_1 can be conducted by the connecting state in Fig. 2(a), which can be achieved by $\overrightarrow{u_3}$ or $\overrightarrow{u_7}(111)$. However, regarding Fig. 3(b), $\overrightarrow{u_3}$ is excluded from the active vectors when $V_{bemfa} > 0$. Hence, $\overrightarrow{u_7}$ can conduct D_1, and its acting time is the conduction time of the negative nonzero current when $V_{bemfa} < (1/3)V_{dc}$.

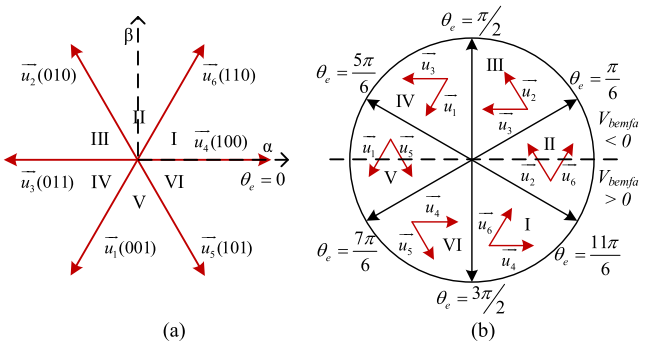

Fig. 3. (a) Voltage vectors and (b) their active phase ranges.

Additionally, according to (11), if $V_{bemfa} > (V_{dc}/3)$, the connecting states in Fig. 2(c) and (d) can also conduct D_1. Regarding Fig. 3(b), the conditions in Fig. 2(c) and (d) can be implemented by $\overrightarrow{u_5}$ in sector VI and $\overrightarrow{u_6}$ in sector I, respectively. Moreover, with the increase in ω_e and V_{bemfa}, both active vectors in sectors II and V can conduct D_1. Therefore, at high speed levels, the conduction time of the nonzero current includes the acting time of $\overrightarrow{u_7}$ and a part or all of the acting time of active vectors in accordance with the sector.

Similarly, because $\overrightarrow{u_4}$ is inactive when $V_{bemfa} < 0$, the positive nonzero current can be conducted through D_2 by $\overrightarrow{u_0}$(000) at any speed level when $V_{bemfa} < 0$. In addition, the dead time T_d occurs on the edges of PWM signals and reduces the acting time of the high-level signals. Therefore, T_d brings extra time for D_2 conduction and compresses the conduction time of D_1. Furthermore, $\overrightarrow{u_5}$, $\overrightarrow{u_6}$, $\overrightarrow{u_1}$ and $\overrightarrow{u_2}$ can conduct D_2 when $V_{bemfa} < -(V_{dc}/3)$. Conclusively, the conduction time of the nonzero current is summarized in Table I, where Δt_{D1} and Δt_{D2} are the conduction times of D_1 and D_2, respectively, and T_{ux} is the acting time of voltage vector $\overrightarrow{u_x}$.

By far, the conduction conditions of the two diodes (D_1 and D_2) in the Phase A leg are studied and the voltage vectors that activate the conduction are revealed. The analysis can be applied to the power switches in other inverter legs.

Like the postfault conduction of phase A, the conduction of the diodes in phases B and C is determined by the back-electromagnetic forces V_{bemfb} and V_{bemfc}. In terms of D_3 and D_4 in the phase B, when $0 < |V_{bemfb}| < V_{dc}/3$, D_3 and D_4 can be conducted by $\overrightarrow{u_7}$ and $\overrightarrow{u_0}$, respectively, because $\overrightarrow{u_5}$ is excluded when $V_{bemfb} > 0$ while $\overrightarrow{u_2}$ is excluded when $V_{bemfb} < 0$ and when; when $|V_{bemfb}| > V_{dc}/3$, D_3 and D_4 can also be conducted by $\overrightarrow{u_3}$, $\overrightarrow{u_6}$, $\overrightarrow{u_1}$ and $\overrightarrow{u_4}$. Regarding the conduction of D_5 and D_6 in the phase C, when $0 < |V_{bemfc}| < V_{dc}/3$, $\overrightarrow{u_7}$ and $\overrightarrow{u_0}$ applies to the conduction of D_5 and D_6, while $\overrightarrow{u_2}$, $\overrightarrow{u_4}$, $\overrightarrow{u_5}$ and $\overrightarrow{u_3}$ can also conduct D_5 and D_6 when $|V_{bemfc}| > V_{dc}/3$.

Before and after the fault occurs, FOC and SVPWM are adopted for the PMSM control and the controller parameters are consistent. It should be noted that the conduction time can also be obtained in other control methods adopting the PWM principle. Although the occurrence of the activating switching states and their acting time can be conveniently determined according to the sector in FOC, they can also be obtained according to the duty ratio of each phase. Once the duty ratios are calculated by the controller, the switching states that are going to be implemented are determined. Denoting the minimum, medium, and maximum duty ratios as $DR_{\min}$, DR_{med}, and $DR_{\max}$, the acting time of $\overrightarrow{u_0}$ and $\overrightarrow{u_7}$ can be calculated as (1- $DR_{\max}$)$*T_s$ and $DR_{\min}*T_s$. The acting time of the other switching states can also be obtained by the duty ratios. Taking the switching state "101" ($\overrightarrow{u_5}$ in SVPWM) as an example, its acting time can be calculated as (DR_{med} - $DR_{\min}$)$*T_s$.

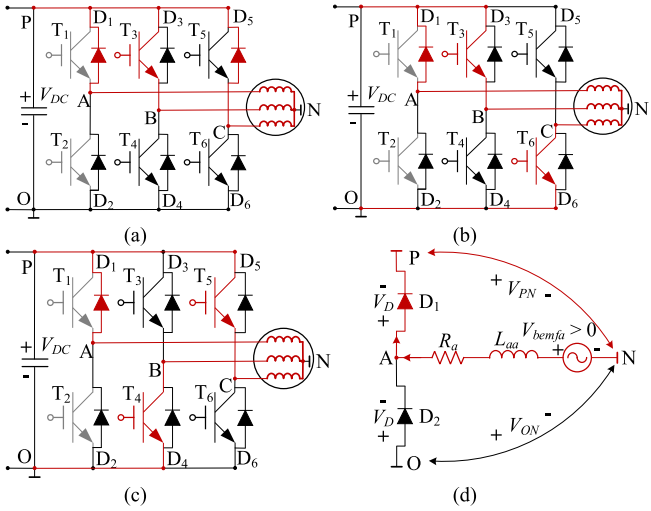

Fig. 4. Connecting states of D_1 conduction when applying (a) $\overrightarrow{u_7}$, (b) $\overrightarrow{u_6}$ or $\overrightarrow{u_2}$, (c) $\overrightarrow{u_5}$ or $\overrightarrow{u_1}$, and (d) equivalent circuit of D_1 conduction.

B. Current Estimation Model Based on Postfault Equivalent Circuits

After discussing the conduction conditions and conduction time of the postfault nonzero current, its model can be established for two purposes: a) the nonzero current can be estimated by the model to validate the correctness of the analysis; b) the estimated value can be employed for further utilization such as diagnosing the open-switch fault and estimating the rotor position [20].

When D_1 is conducting, the connecting states and equivalent circuit of the faulty phase can be depicted in Fig. 4.

Defining the current that flows to the winding as positive, according to Fig. 4(d), the following equations can be obtained according to Kirchhoff's voltage law:

$$-V_{bemfa} - L_{aa}di_a/dt - R_a i_a + V_{PN} = 0. \tag{16}$$

Although i_b is not strictly equal to $-i_c$ when the postfault i_a is conducting, the voltages induced by L_{ab} and L_{ac} in (1) can be considered mutually canceled and are negligible as a part of the voltage source compared with V_{bemfa}. Another reason for neglecting the mutual inductance in modeling the nonzero current is to avoid errors from the sampling process of i_b and i_c. $R_a i_a$ is also negligible compared to V_{bemfa}.

Furthermore, the connecting state in Fig. 4(a) is equivalent to the connecting state by applying $\overrightarrow{u_7}$ under the healthy condition, where $V_{PN} = 0$ and $V_{NO} = V_{dc}$, while the connecting states in

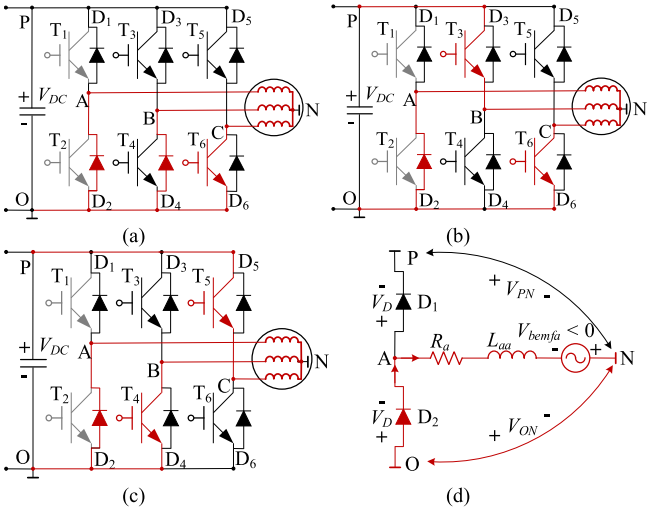

Fig. 5. Connecting states of D_2 conduction when applying (a) $\overrightarrow{u_0}$, (b) $\overrightarrow{u_6}$ or $\overrightarrow{u_2}$, (c) $\overrightarrow{u_5}$ or $\overrightarrow{u_1}$, and (d) equivalent circuit of D_2 conduction.

Fig. 4(b) and (c) are equivalent to applying $\overrightarrow{u_6}$ and $\overrightarrow{u_5}$ under the healthy condition in which $V_{PN} = V_{dc}/3$ and $V_{ON} = -2V_{dc}/3$. Then, (16) can be transformed into

$$V_{bemfa} - V_{PN} = -L_{aa}di_a/dt = \begin{cases} V_{bemfa},\ 0 < V_{bemfa} < \frac{V_{dc}}{3} \\ V_{bemfa} - \frac{V_{dc}}{3},\ \frac{V_{dc}}{3} < V_{bemfa} \end{cases}. \tag{17}$$

When D_2 is conducting, the connecting states and equivalent circuits are shown in Fig. 5.

Similarly, the situation when D_2 is conducted can be described by the following equation:

$$-|V_{bemfa}| - V_{ON} + R_a i_a + L_{aa}di_a/dt = 0. \tag{18}$$

In (18), $|V_{bemfa}| = -V_{bemfa}$ holds since $V_{bemfa} < 0$. In Fig. 5(a), $V_{ON} = 0$ and $V_{PN} = V_{dc}$, while $V_{ON} = -V_{dc}/3$ and $V_{PN} = 2V_{dc}/3$ in Fig. 5(c) and (d). Hence, (18) is transformed into the following equation:

$$-V_{bemfa} + V_{ON} = L_{aa}di_a/dt = \begin{cases} -V_{bemfa}, 0 > V_{bemfa} > -\frac{V_{dc}}{3} \\ -V_{bemfa} - \frac{V_{dc}}{3},\ -\frac{V_{dc}}{3} > V_{bemfa} \end{cases}. \tag{19}$$

Introducing the conduction time summarized in Table I to (17) and (19), the postfault current can be calculated in (20) where Δi_a is the current increment generated in each switching cycle and is equal to the nonzero current because the nonzero current increases from 0 at the beginning of its conduction time. In (20), for simplicity, $T_{u7\_d} = T_{u7} - T_d$ and $T_{u0\_d} = T_{u0} + T_d$ are defined.

$$i_{a\_cal} = \Delta i_a = \begin{cases} \frac{-(V_{bemfa} - \frac{V_{dc}}{3}) * (\Delta t_{D1} - T_{u7\_d}) - V_{bemfa} * T_{u7\_d}}{L_{aa}},\ \frac{V_{dc}}{3} \\ \qquad\qquad < V_{bemfa} \\ -V_{bemfa} * T_{u7\_d}/L_{aa}, 0 < V_{bemfa} < \frac{V_{dc}}{3} \\ -V_{bemfa} * T_{u0\_d}/L_{aa}, 0 > V_{bemfa} > -\frac{V_{dc}}{3} \\ \frac{(-V_{bemfa} - \frac{V_{dc}}{3}) * (\Delta t_{D2} - T_{u0\_d}) - V_{bemfa} * T_{u0\_d}}{L_{aa}}, -\frac{V_{dc}}{3} \\ \qquad\qquad > V_{bemfa} \end{cases}. \tag{20}$$

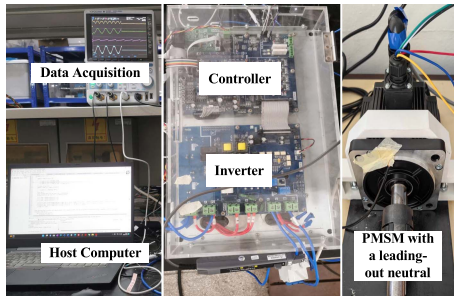

Fig. 6. Experimental setups.

It is important to note that this article focuses on analyzing the mechanism and developing a calculation model for the open-circuit current in surface-mounted PMSM drives. Regarding the salient motor, due to the saliency, the phase self-inductances and mutual-inductances fluctuate with the rotor position. Consequently, the current dynamics of the remaining healthy phases also contribute to the current dynamic of the faulty phase. The impact of the currents in healthy phases on the open-circuit current increases with the rotor saliency, as larger inductance fluctuation results in a greater effect.

IV. Validation

To validate the analysis and the real-time calculating capability of the proposed model, a standard PMSM drive with a leading-out neutral point was employed, as shown in Fig. 6. A Resolver-to-Digital converter (RDC) is equipped to sample the mechanical angle information from the rotor. The controller is based on TMS320F28335, capable of controlling the PWM signals separately, and employs a 4-channel digital-to-analog (0 $\sim$ 5 V analog output) converter (DAC) to transmit data from the controller to the oscilloscope for data acquisition at the switching frequency. The data transmitted via DAC includes q-axis current, the calculated conduction time, the speed feedback, the calculated V_{bemfa}, and the calculated postfault current i_{a_cal}. Additionally, current probes (*Cybertek* CP8050A, 50 MHz) and voltage probes (*Tektronix* P5200, 50 MHz) are used for measurement. The inverter works at 10 kHz and is supplied by 200 V dc. The parameters of the PMSM are shown in Table II.

The employed power switch is IGBT *FUJI* 7MBR25VA120-50. However, it should be noted that, unlike the Si and SiC devices, GaN devices do not need antiparallel diodes for reverse conduction due to the symmetrical structure. Similar to its forward conduction, when the gate-to-drain voltage V_{gd} is greater than the threshold voltage V_{th}, the reverse conduction of the

TABLE II
PARAMETERS OF THE PMSM

Parameter	Value
Number of pole pairs	4
Resistance of stator	1.32 Ω
d axis inductance	3.21 mH
q axis inductance	3.21 mH
The flux of the rotor	0.1467 Wb
Rated power	750 W
Rated speed	1800 rpm
Rated torque	4 N.m

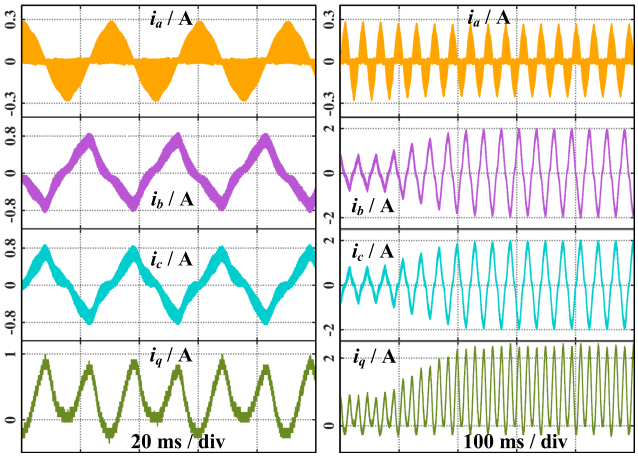

Fig. 7. Postfault current responses at 500 rpm under (a) no load torque and (b) variable load torque.

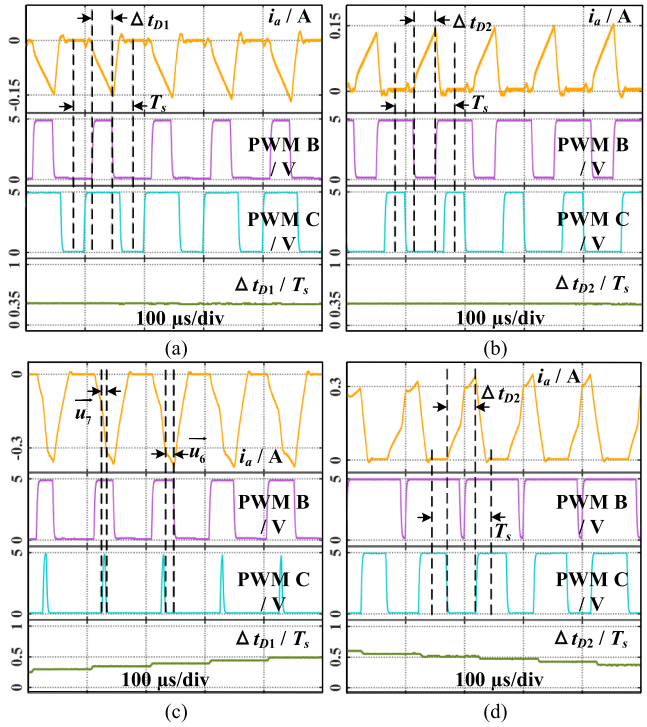

Fig. 8. Postfault i_a, PWM B&C, and conduction time in each switching cycle at (a) and (b) 500 rpm and (c) and (d) 1500 rpm when (a) and (c) $V_{bemfa} > 0$ and (b) and (d) $V_{bemfa} < 0$.

GaN device can be achieved. In terms of the open-switch fault incurred by missing driving signals, the gate-to-source voltage V_{gs} is equal to 0 V because the gate leakage current is negligible [24], and V_{gd} is equal to the source-to-drain voltage V_{sd} because $V_{gd} = V_{gs} + V_{sd} = V_{sd}$. V_{sd} is equal to V_{AP} or V_{OA} in case of discussing the postfault conduction of the upper half leg or the lower half leg. Therefore, substituting the forward on-voltage of the reverse diode V_D by V_{th}, the conduction conditions analyzed in Section II-A can be applied to the postfault reverse conduction of GaN devices.

Nevertheless, in GaN-based motor drives, both the damaged power switches and disconnections of motor phases will not allow the studied open-circuit current to conduct. In this case, the studied open-circuit current can still be activated when the fault is incurred by missing driving signals and can be employed to distinguish this type of open-circuit fault from others.

A. Validation of the Conduction Conditions and Conduction Time

In Fig. 7, the postfault i_a is discontinuous, which verifies that it is related to the switching state. Additionally, at the same speed level, the change in load torque does not directly influence the envelope and amplitude of the postfault i_a because its voltage source is $V_{bemfa,}$ which is determined by the rotor speed and does not relate to the load torque, as analyzed in Section II. In Fig. 7(b), when the load varies, the amplitude of i_a slightly changes due to the slight change in speed posed by the variable torque.

To prove the analysis of the conduction time in Section II-B, i_a and its conduction time are presented in Fig. 8 in accordance with switching states. In Fig. 8(a) and (b), the motor operates at 500 rpm, where the peak value of V_{bemfa} (approximately 30 V) is lower than that of $V_{dc}/3$ (approximately 66.6 V). As analyzed in Section II-A and summarized in Table I, when $|V_{bemfa}| < V_{dc}/3$, D_1 is conducted only when $\overrightarrow{u_7}$ is being applied while $\overrightarrow{u_0}$ conducts D_2. The ratio of the conduction time accounts for 35% of the entire switching cycle and relatively slowly changes in each cycle because the flux controlled at low speed can stay in each sector for a relatively long time.

Comparatively, at the high speed level in Fig. 8(c) and (d), the conduction time has noticeable changes in each cycle because the duty ratios of the driving signals rapidly change. Unlike the behaviors at 500 rpm, when the speed is lifted to 1500 rpm, where V_{bemfa} (approximately 92 V amplitude) can be higher than $V_{dc}/3$, D_1 and D_2 are conducted in $\overrightarrow{u_7}$, $\overrightarrow{u_0}$ and other vectors that separately connect phases B and C to the positive and negative rails, corresponding to the analysis of Section II. Additionally, as described in (20), i_a has a higher changing rate in the zero vectors than other vectors because of different values of the voltage source.

In addition, i_a maintains its conduction for a short period after removing its activation switching state at both speed levels. For example, in Fig. 8(c), i_a converges to zero while maintaining conduction after removing $\overrightarrow{u_6}$. In this case, the connecting state

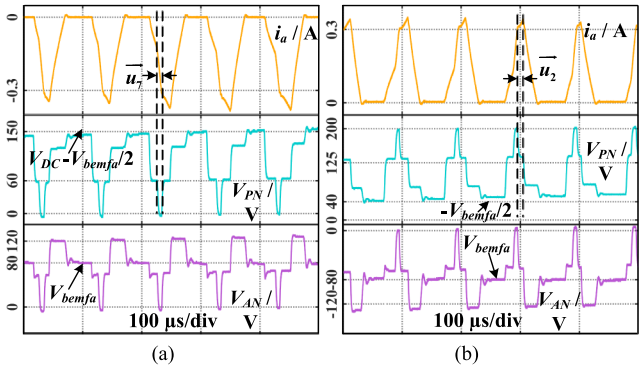

Fig. 9. Postfault i_a, V_{PN}, and V_{AN} in each switching cycle at 1500 rpm when (a) $V_{bemfa} > 0$ and (b) $V_{bemfa} < 0$.

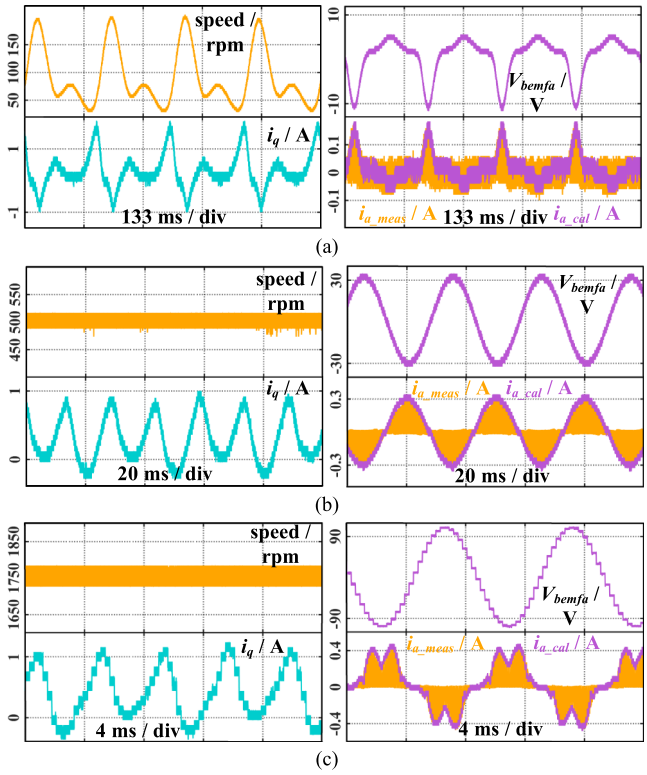

Fig. 10. Postfault speed, V_{bemfa}, i_{a_cal}, i_{a_meas} at (a) 90 rpm, (b) 500 rpm, and (c) 1800 rpm.

is equivalent to Fig. 2(b), where negative i_a cannot be activated. This nonactivated conduction is caused by the free-wheeling effect due to the winding inductance. During this period, the faulty phase is still conducting, and the effect of the voltage vector is equivalent to the prefault state.

The states of V_{PN} and V_{AN} at 1500 rpm are shown in Fig. 9. In Fig. 9(a), as shown in Fig. 8(c), $\overrightarrow{u_4}$ and $\overrightarrow{u_0}$ are applied when i_a is not conducting, which corresponds to the connecting state in Fig. 2(b). In this case, $V_{AN} = V_{bemfa}$ (approximately 92 V amplitude) and $V_{PN} = V_{dc} - V_{bemfa}/2$, which validates the analysis in (6). Similarly, in Fig. 9(b), the connecting state when i_a is not conducting corresponds to Fig. 2(a), where $V_{PN} = -V_{bemfa}/2$.

When i_a is conducting, the connecting states are equivalent to the states under healthy conditions. For example, when the positive i_a is conducted by $\overrightarrow{u_2}$, as shown in Fig. 9(b), phase A is connected to the negative rail through D_2, and the connecting state is equivalent to the state of applying $\overrightarrow{u_2}$ under the healthy condition where $V_{PN} = V_{BN} = 2V_{dc}/3$ and $V_{AN} = -V_{dc}/3$. Furthermore, when $\overrightarrow{u_7}$ is conducting the negative i_a through D_1, as shown in Fig. 9(a), the connecting state is identical to applying $\overrightarrow{u_7}$ under the healthy condition where $V_{PN} = 0$. However, unlike the healthy condition, i_a is activated by $V_{bemfa} - V_{PN}$, instead of V_{dc} under the healthy condition. Therefore, although the voltages at terminal A and neutral point N have been clamped to the same level when i_a is conducting, the voltage source in phase still exists to activate the postfault i_a, as described in Figs. 4(d) and 5(d).

B. Validation of the Proposed Current Estimation Model

Based on the estimation model proposed in (20), the postfault i_a can be calculated by the controller in real time, denoted as i_{a_cal}, and compared with the measured current i_{a_meas}, as shown in Fig. 10. In Fig. 10(b) and (c), although i_q severely fluctuates at both speed levels, the open-switch fault does not affect the speed, and V_{bemfa} maintains the sinusoidal pattern. The open-switch fault affects the speed by changing the voltage vectors, and the severity of the effect is influenced by the rotor inertia, speed level, and load torque. In summary, the speed is prone to be slightly affected by the fault when the motor is operating at high speed, with light load torque and large inertia. In terms of the high speed, the time when the flux is controlled by the influenced voltage vectors is shortened, and the speed cannot respond to the rapidly changing i_q because the mechanical time constant is much larger than the electrical time constant.

Different from the constant motor speed in Fig. 10(b) and (c), the motor speed in Fig. 10(a) severely fluctuates when the speed command is 5% (90 rpm) of its rated speed. The reason lies in that, at low speed levels, the motor operates for an extended period of time within the phase range affected by the fault. As a result, the time of i_q fluctuation is longer than that of high speed levels and it allows the mechanical shaft to respond to the i_q fluctuation.

In Fig. 10(b), V_{bemfa} is less than $V_{dc}/3$ and acts as the only excitation source of the open-circuit current, and both i_{a_meas} and i_{a_cal} follow the sinusoidal pattern of V_{bemfa}. In Fig. 10(a), where V_{bemfa} is also less than $V_{dc}/3$, although the amplitude of V_{bemfa} is small, i_{a_meas} still follows the pattern of V_{bemfa} in reverse because it shares the same activation mechanism with the open-switch current in Fig. 10(b). However, when the motor is operating at the nominal speed, the postfault i_a does not follow the pattern of V_{bemfa} and has a sag when V_{bemfa} is around its peak value. The reason for the current sag is explained as follows: when V_{bemfa} is around its peak where θ_e is approximately $\pi/2$ or $3\pi/2$, the controlled flux is on the boundary of sectors III and IV or sectors VI and I, as shown in Fig. 3(b). On the boundaries, $\overrightarrow{u_3}$ or $\overrightarrow{u_4}$ are the dominant active vectors that account for most of the acting time in each switching cycle, and they cannot activate the

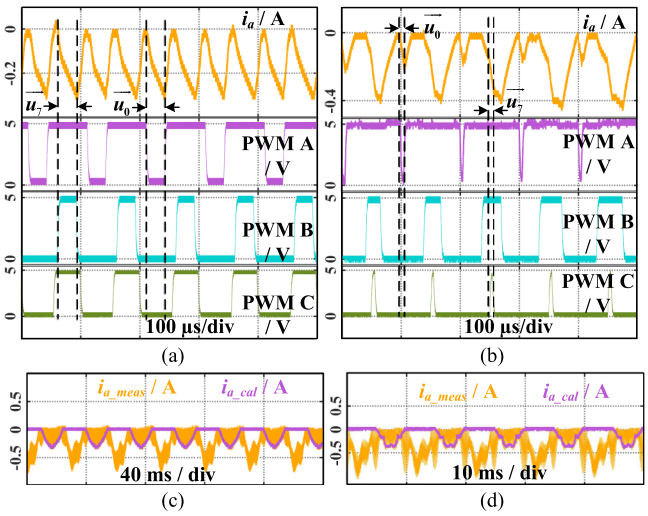

Fig. 11. T_1 single open-switch i_a and PWM signals in each switching cycle at (a) 500 rpm and (b) 1500 rpm. Comparison of i_{a_meas} and i_{a_cal} at (c) 500 rpm and (d) 1500 rpm.

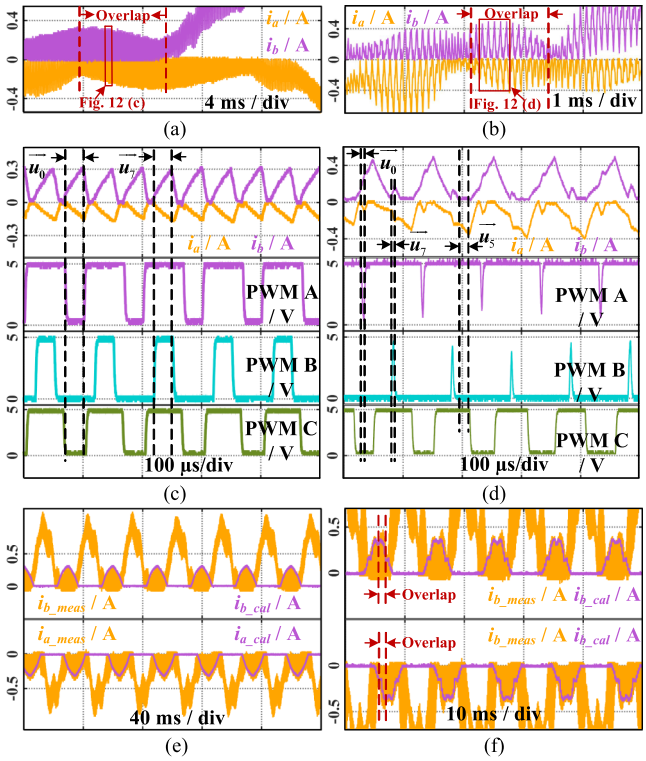

Fig. 12. T_1&T_4 open-switch currents at (a) 500 rpm and (b) 1500 rpm. Currents and PWM signals in each switching cycle at (c) 500 rpm and (d) 1500 rpm. Comparison of measurement and calculation at (e) 500 rpm and (f) 1500 rpm.

postfault i_a. Meanwhile, the acting time of zero vectors accounts for a small portion of the switching period at high speed levels, as shown in Fig. 8(c) and (d). Therefore, when V_{bemfa} is around its peak values at high speed levels, the amplitude of the postfault i_a decreases because its conduction is squeezed by $\overrightarrow{u_3}$ or $\overrightarrow{u_4}$.

At different speed and V_{bemfa} levels, i_{a_cal} and i_{a_meas} are compared in the last scopes of Fig. 10(a)–(c). Because the voltage source and conduction time are comprehensively considered in (20), the calculated value matches the pattern and amplitude of the measured value on the scale of milliamperes in real time, which validates the effectiveness of the proposed model. In addition, it should be noted that the digital controller only executes the embedded codes once per switching cycle. As a result, the calculated current is updated only once per switching cycle, rather than following the discontinuous switching states within each cycle. Therefore, the calculation result presents the continuous envelop of the open-switch current, rather than the current pulses within each switching cycle.

C. Tests and Analysis of Single Open-Switch Fault

The feasibility of the proposed model is also tested for the other types of faults, including T_1 single open-switch fault, and T_1&T_4 multiphase open-switch fault.

Regarding the T_1 single open-switch fault, the activation mechanism of the postfault i_a conducting through D_1 does not change and can be concluded as when $0 < V_{bemfa} < V_{dc}/3$, D_1 can be conducted by $\overrightarrow{u_7}$ which connects both phase B and phase C to the positive dc rail; when $V_{bemfa} > V_{dc}/3$, D_1 can also be conducted by $\overrightarrow{u_1}$, $\overrightarrow{u_2}$, $\overrightarrow{u_5}$, and $\overrightarrow{u_6}$ which connect phase B and phase C to the positive and negative dc rails separately.

Different from the fault with two faulty switches in the same phase, because of the still-functional T_2, the open-switch i_a can also conduct through T_2 by $\overrightarrow{u_0}$ when $V_{bemfa} > 0$, as shown in Fig. 11(a) and (b). However, the extra current path does not affect the amplitude of the open-switch current. When the current is activated by $\overrightarrow{u_0}$, it has the identical activation source V_{bemfa} as the open-switch current activated by $\overrightarrow{u_7}$. On the other hand, the acting time $\overrightarrow{u_0}$ is the same as that of $\overrightarrow{u_7}$ in symmetric PWM control. Therefore, the proposed model is also applicable to the single open-switch fault. The validation of the case of single open-switch fault is presented in Fig. 11(c) and (d), in which i_{a_cal} still matches the amplitude of i_{a_meas} in the faulty half.

D. Tests and Analysis of Faults in Different Phases

Taking the fault in which T_1 and T_4 are disabled as an example. The faulty T_1 affects the phase A current when $V_{bemfa} > 0$, while the faulty T_4 affects the phase B current when $V_{bemfb} < 0$. The open-switch i_a and i_b have an overlapping area as depicted in Fig. 12(a) and (b), while they have independent mechanisms in the rest of their faulty phase ranges.

In the overlapping area depicted in Fig. 12(a), when the amplitudes of V_{bemfa} and V_{bemfb} are less than $V_{dc}/3$, the proposed model is still effective for each phase and the faulty current of each phase is the same as the single open-switch current of each phase. As analyzed in the case of single open-switch fault, both the $\overrightarrow{u_7}$ and $\overrightarrow{u_0}$ can conduct the same amplitude open-switch i_a through D_1 or T_2. It also applies to the open-switch i_b. When $\overrightarrow{u_7}$ is being applied, the open-switch i_a is conducting through D_1 while the open-switch i_b can conduct through the remaining healthy T_3. Similarly, when $\overrightarrow{u_0}$ is being applied, the open-switch i_b conducts through D_4 while the open-switch i_a conducts

through the healthy T_2, as shown in Fig. 12(c). Therefore, the overlapping area does not affect the calculation result of the proposed model when the amplitudes of V_{bemfa} and V_{bemfb} are less than $V_{dc}/3$, as validated in Fig. 12(e).

Nevertheless, the conduction mechanism becomes more complex when the amplitudes of V_{bemfa} and V_{bemfb} exceed $V_{dc}/3$, where the nonzero vectors are also involved. In the overlapping area depicted in Fig. 12(b) and when the nonzero vector ($\overrightarrow{u_5}$) is being applied, the phase A and C have been connected to the positive dc rail. In this case, the postfault i_b cannot conduct through D_4 since $V_{bemfb} > (2V_{dc}/3)$ cannot be achieved as analyzed in Section II-A and shown in Fig. 12(d). Therefore, the postfault i_a can no longer be calculated based on the established excitation source and conduction time, but is related to the value of i_c. As a result, when V_{bemfa} and V_{bemfb} exceed $V_{dc}/3$, the calculated open-switch currents do not completely match the measured currents in the overlapping area, whereas the proposed model is still effective in the nonoverlapping area, as shown in Fig. 12(f).

Conclusively, the proposed model is still effective under the single open-switch fault, the nonoverlapping area of the multiphase open-switch fault, and the overlapping area of the multiphase fault when the back-electromagnetic forces are less than $V_{dc}/3$. Regarding the overlapping area of the multiphase fault when the back-electromagnetic forces exceed $V_{dc}/3$, the conduction mechanism of open-switch current has changed when the nonzero vectors are being applied and results in the mismatch between the calculation and measurement.

V. Discussion

The analysis and experimental results have validated that the open circuit with functional and dysfunctional antiparallel diodes have different postfault phase voltages and currents. Therefore, before developing the methods to diagnose and tolerate the different faults, the postfault model and mechanism need to be established and revealed at the first place.

The application of the proposed model in the diagnosis and fault-tolerant control will be discussed since the diagnosis and tolerant control are the most direct applications of the proposed model. However, the proposed model also has the potential to be utilized in other scenarios, such as estimating or calibrating the rotor position and flux parameter since it is validated that the open-circuit current is directly activated by the back-electromagnetic force and is closely related to the electric angle.

A. Diagnosis Method for Identifying Open-Circuit Faults With Functional and Dysfunctional Diodes

The open-circuit phase with functional and dysfunctional free-wheeling diodes are incurred by different failures and have different postfault characteristics. Different postfault characteristics result in different fault-tolerant control methods and are required to be identified.

According to the proposed model and the revealed mechanism, the most significant postfault state, the open-circuit current, can be estimated and sampled.

1) Sampling of the Open-Circuit Current: Based on the activating switching states identified in Section III-A, the information of the postfault current can be acquired by current sampling, rather than measuring it by current probe.

Typically, the phase current is sampled at the midpoint of $\overrightarrow{u_0}$ to obtain the average value of current ripples. In this way, half the amplitude of the positive half-cycle open-circuit current can be sampled because the midpoint of $\overrightarrow{u_0}$ happens to be the midpoint of the increasing positive open-circuit current, as shown in Fig. 8(b) and (d), while the negative part of the open-circuit current cannot be acquired.

To obtain the full amplitude of the open-circuit current, the sampling point needs to be adjusted. When $|V_{bemfa}| < V_{dc}/3$, the positive or negative amplitude of the open-circuit current should be sampled at the ending point of $\overrightarrow{u_0}$ or $\overrightarrow{u_7}$, as shown in Fig. 8(b) and (a), respectively. When $|V_{bemfa}| > V_{dc}/3$, the amplitude should be sampled at the ending points of the activating switching states corresponding to Table I. For example, when the flux is being controlled by the voltage vectors in space sector I, the negative peak of the open-circuit current can be sampled at the second ending point of $\overrightarrow{u_6}$.

2) Diagnosis of Open-Circuit Faults With Functional and Dysfunctional Diodes: After obtaining the estimated and sampled values of the open-circuit current, the existing model-based and data-driven methods referred to in this article can be implemented. Taking the data-driven method in [8] as an example, the errors between the estimated and sampled currents have different data structures under the health condition, the open-circuit fault with functional diodes, and the open-circuit fault with dysfunctional diodes. Therefore, data-driven classifiers can be trained and operated online based on the different data structures of the errors to realize the diagnosis.

B. Fault-Tolerant Control Methods for Improving the Postfault Performance of PMSM Drives

After identifying the fault state of the motor drive, fault-tolerant methods can be designed to maintain the postfault performance. Based on the proposed model, the open-circuit fault-tolerant control can be implemented from multiple aspects.

One of the aspects is modifying the modulation scheme. As described in Section II, the open-circuit fault with functional diodes has fixed phase voltages when the activation switching states are being applied, while the fault with dysfunctional diodes has floating phase voltages depending on the phase back-electromagnetic force. In both fault states, the inverter voltage vectors have changed in their amplitudes and phases. Therefore, the modulation scheme, especially the acting time of each vector, can be adjusted to adapt to the changes in postfault voltage vectors.

On the other hand, instead of adjusting the modulation method of FOC, the proposed model can also be employed in fault-tolerant model predictive control. Since the detailed model of the postfault system has been proposed, the healthy model of the motor drive can be substituted by the postfault model after the detection of the fault to predict the postfault system behaviors.

VI. Conclusion

The unknown mechanism of the nonzero open-circuit current is revealed in this article. The postfault behaviors have been analyzed, and the corresponding equivalent circuits are provided. Moreover, switching patterns that fulfill the conduction condition are determined to confirm the conduction time. Finally, the model of the nonzero current is given and experimentally validated. The revealed mechanism and proposed model can be employed to distinguish open-circuit faults and open-phase faults and for further utilization. Additionally, the proposed model can be further studied by incorporating the back-EMF and inductances of multiphase motor drives.

References

[1] S. Yang, A. Bryant, P. Mawby, D. Xiang, L. Ran, and P. Tavner, "An industry-based survey of reliability in power electronic converters," *IEEE Trans. Ind. Appl.*, vol. 47, no. 3, pp. 1441–1451, May/Jun. 2011.

[2] J. He, N. A. O. Demerdash, N. Weise, and R. Katebi, "A fast on-line diagnostic method for open-circuit switch faults in SiC-MOSFET-based T-type multilevel inverters," *IEEE Trans. Ind. Appl.*, vol. 53, no. 3, pp. 2948–2958, May/Jun. 2017.

[3] X. Wang, Z. Wang, M. Gu, B. Wang, W. Wang, and M. Cheng, "Current optimization-based fault-tolerant control of standard three-phase PMSM drives," *IEEE Trans. Energy Convers.*, vol. 36, no. 2, pp. 1023–1035, Jun. 2021.

[4] K. Hu, Z. Liu, Y. Yang, F. Iannuzzo, and F. Blaabjerg, "Ensuring a reliable operation of two-level IGBT-based power converters: A review of monitoring and fault-tolerant approaches," *IEEE Access*, vol. 8, pp. 89988–90022, 2020.

[5] V. John, B.-S. Suh, and T. A. Lipo, "Fast-clamped short-circuit protection of IGBT's," *IEEE Trans. Ind. Appl.*, vol. 35, no. 2, pp. 477–486, Mar./Apr. 1999.

[6] R. Wu, F. Blaabjerg, H. Wang, M. Liserre, and F. Iannuzzo, "Catastrophic failure and fault-tolerant design of IGBT power electronic converters - an overview," in *Proc. 39th Annu. Conf. IEEE Ind. Electron. Soc.*, 2013, pp. 507–513, doi: 10.1109/iecon.2013.6699187.

[7] W. Huang, J. Du, W. Hua, K. Bi, and Q. Fan, "A hybrid model-based diagnosis approach for open-switch faults in PMSM drives," *IEEE Trans. Power Electron.*, vol. 37, no. 4, pp. 3728–3732, Apr. 2022.

[8] Z. Zhang, G. Luo, Z. Zhang, and X. Tao, "A hybrid diagnosis method for inverter open-circuit faults in PMSM drives," *CES Trans. Elect. Mach. Syst.*, vol. 4, no. 3, pp. 180–189, Sep. 2020.

[9] S. Yin, S. X. Ding, X. Xie, and H. Luo, "A review on basic data-driven approaches for industrial process monitoring," *IEEE Trans. Ind. Electron.*, vol. 61, no. 11, pp. 6418–6428, Nov. 2014.

[10] L. Wen, X. Li, L. Gao, and Y. Zhang, "A new convolutional neural network-based data-driven fault diagnosis method," *IEEE Trans. Ind. Electron.*, vol. 65, no. 7, pp. 5990–5998, Jul. 2018.

[11] X. Wang, Z. Wang, Z. Xu, J. He, and W. Zhao, "Diagnosis and tolerance of common electrical faults in T-type three-level inverters fed dual three-phase PMSM drives," *IEEE Trans. Power Electron.*, vol. 35, no. 2, pp. 1753–1769, Feb. 2020.

[12] Z. Wang, J. Chen, M. Cheng, and Y. Zheng, "Fault-tolerant control of paralleled-voltage-source-inverter-fed PMSM drives," *IEEE Trans. Ind. Electron.*, vol. 62, no. 8, pp. 4749–4760, Aug. 2015.

[13] Z. Zhang, Y. Hu, G. Luo, C. Gong, X. Liu, and S. Chen, "An embedded fault-tolerant control method for single open-switch faults in standard PMSM drives," *IEEE Trans. Power Electron.*, vol. 37, no. 7, pp. 8476–8487, Jul. 2022.

[14] H. Chen, J. He, N. A. O. Demerdash, X. Guan, and C. H. T. Lee, "Diagnosis of open-phase faults for a five-phase PMSM fed by a closed-loop vector-controlled drive based on magnetic field pendulous oscillation technique," *IEEE Trans. Ind. Electron.*, vol. 68, no. 7, pp. 5582–5593, Jul. 2021.

[15] H. Guzman, M. J. Duran, F. Barrero, B. Bogado, and S. Toral, "Speed control of five-phase induction motors with integrated open-phase fault operation using model-based predictive current control techniques," *IEEE Trans. Ind. Electron.*, vol. 61, no. 9, pp. 4474–4484, Sep. 2014.

[16] C. M. Hackl, U. Pecha, and K. Schechner, "Modeling and control of permanent-magnet synchronous generators under open-switch converter faults," *IEEE Trans. Power Electron.*, vol. 34, no. 3, pp. 2966–2979, Mar. 2019.

[17] H. Guzmán, J. A. Riveros, M. J. Durán, and F. Barrero, "Modeling of a five-phase induction motor drive with a faulty phase," in *Proc. 15th Int. Power Electron. Motion Control Conf.*, 2012, pp. LS1c.3-1–LS1c.3-6, doi: 10.1109/epepemc.2012.6397393.

[18] H. Guzman, F. Barrero, and M. J. Duran, "IGBT-gating failure effect on a fault-tolerant predictive current-controlled five-phase induction motor drive," *IEEE Trans. Ind. Electron.*, vol. 62, no. 1, pp. 15–20, Jan. 2015.

[19] U. Pecha, N. Parspour, and F. Gieck, "Modeling and analysis of multiple open-switch faults in converters supplying permanent-magnet synchronous machines," in *Proc. IEEE 13th Int. Symp. Diagnostics Elect. Mach., Power Electron. Drives*, 2021, pp. 240–246, doi: 10.1109/sdemped51010.2021.9605533.

[20] B. Tian, M. Molinas, Q. An, B. Zhou, and J. Wei, "Freewheeling current-based sensorless field-oriented control of five-phase permanent magnet synchronous motors under insulated gate bipolar transistor failures of a single phase," *IEEE Trans. Ind. Electron.*, vol. 69, no. 1, pp. 213–224, Jan. 2022.

[21] C. Gong, Y. Hu, C. Gan, G. Chen, and M. Alkahtani, "Modeling, analysis, and attenuation of uncontrolled generation for IPMSM-based electric vehicles in emergency," *IEEE Trans. Ind. Electron.*, vol. 67, no. 6, pp. 4453–4462, Jun. 2020.

[22] H. A. A. Awan, M. Hinkkanen, R. Bojoi, and G. Pellegrino, "Stator-flux-oriented control of synchronous motors: A systematic design procedure," *IEEE Trans. Ind. Appl.*, vol. 55, no. 5, pp. 4811–4820, Sep./Oct. 2019.

[23] A. K. Jain and V. T. Ranganathan, "Modeling and field oriented control of salient pole wound field synchronous machine in stator flux coordinates," *IEEE Trans. Ind. Electron.*, vol. 58, no. 3, pp. 960–970, Mar. 2011.

[24] K. Wang, X. Yang, L. Wang, and P. Jain, "Instability analysis and oscillation suppression of enhancement-mode GaN devices in half-bridge circuits," *IEEE Trans. Power Electron.*, vol. 33, no. 2, pp. 1585–1596, Feb. 2018.

Zeliang Zhang (Student Member, IEEE) was born in Shaanxi, China, in 1995. He received the B.S. and M.S. degrees in electrical engineering from Northwestern Polytechnical University, Xi'an, China, in 2017 and 2020, respectively. He is currently working toward the Ph.D. degree in electrical engineering with the University of York, York, U.K.

His research interests include fault modeling, diagnosis, and fault-tolerant control in motor drives.

Yihua Hu (Senior Member, IEEE) received the B.S. degree in electrical engineering and the Ph.D. degree in power electronics and drives from the China University of Mining and Technology, Xuzhou, China, in 2003 and 2011, respectively.

From 2011 to 2013, he was with the College of Electrical Engineering, Zhejiang University, Hangzhou, China, as a Postdoctoral Fellow. From 2013 to 2015, he worked as a Research Associate with the Power Electronics and Motor Drive Group, University of Strathclyde, Glasgow, U.K. From 2016 to 2019, he was a Lecturer with the Department of Electrical Engineering and Electronics, University of Liverpool (UoL), Liverpool, U.K. From 2019 to 2023, he was a Reader with Electronics Engineering Department, University of York (UoY), York, U.K. He is currently a Reader with the Department of Engineering, King's College London (KCL), London, U.K. He has authored or coauthored more than 150 papers in IEEE transactions journals. His research interests include renewable generation, power electronics converters and control, electric vehicle, more electric ship/aircraft, smart energy system, and nondestructive test technology.

Dr. Hu is an Associate Editor for the IEEE Transactions on Industrial Electronics, *IET Renewable Power Generation*, *IET Intelligent Transport Systems*, and *Scientific Reports*. He is a Fellow of the Institution of Engineering and Technology (FIET). He was awarded Royal Society Industry Fellowship.

Guangzhao Luo (Senior Member, IEEE) received the M.S. and Ph.D. degrees in electrical engineering from Northwestern Polytechnical University (NPU), Xi'an, China, in 1998 and 2003, respectively.

From 2003 to 2004, he was a Postdoctoral Researcher with the University of Federal Defense, Munich, Germany. He is currently a Professor with NPU. He is also the Vice Director of the Rare Earth Permanent Magnet (REPM) Electric Machine and Control Engineering Center, Shaanxi, China. His research interests include advance control theory of permanent magnet electrical machine, high-performance control technology of permanent magnet synchronous motor for electric traction and electric vehicle, real-time simulation technology for electrical drive systems, and intelligence control of new energy conversion.

Dr. Luo received the Second Prize from the China National Defense Science and Technology Progress Award in 1995 and 2011.

Hui Xu received the B.S. in electrical engineering, M.Eng. in electrical engineering, and Ph.D. degrees in electrical engineering from the China University of Mining and Technology, Beijing, China, in 2005, 2009, and 2012, respectively.

From 2012 to 2013, she was a Postdoctoral Researcher with Zhejiang University. She is currently a Research Assistant in artificial intelligence and energy with Leeds Beckett University, Leeds, U.K.

Chao Gong (Member, IEEE) was born in Shandong, China, on February 22, 1991. He received the B.Eng. and M.Eng. degrees in electrical engineering from Northwestern Polytechnical University, Xi'an, China, in 2014 and 2016, respectively, and the Ph.D. degree in electrical engineering from the University of York, York, U.K., in 2021.

He is currently a Postdoctoral Researcher with the Department of Electrical and Computer Engineering, University of Alberta, Edmonton, AB, Canada. His research interests include electrical machines design and drives, power electronics, and motion control.